Ground state properties of Zn, Ge, and Se isotopic chains in covariant density functional theory

Nihad J. Abu Awwad,[1] H. Abusara,[1,*] and Shakeb Ahmad[2,†]
[1]*Department of Physics, Birzeit University, Birzeit, Palestine*
[2]*Physics Section, Women's College, Aligarh Muslim University, Aligarh 202002, India*

(Received 14 June 2019; revised manuscript received 19 April 2020; accepted 9 June 2020; published 29 June 2020)

A systematic investigation of the ground state deformation, the physical properties (two-neutron separation energy and neutron, proton, and charge radii), and the possibility of nuclear shape coexistence in Zn, Ge, and Se isotopes was performed using the relativistic Hartree-Bogoliubov formalism using density-dependent zero- and finite-range *NN* interactions. Shape coexistence does not show up clearly in Zn isotopes. However, it is clear in most of the Ge and Se isotopes; the two coexistence minima are axial and triaxial in the case of Ge, while both are axial in the case of Se. Along all these chains one can see the existence of several transition points, where the ground state shape suddenly changes. This sudden change affects the evolution of the physical properties. The density of states near the Fermi level is a key factor in determining the ground state minima. Both point-coupling and meson-exchange models give similar results with few exceptions. A very good agreement is found with the available experimental data. The SU(3) proxy provides a reasonable prediction of the deformation value in the middle of the isotopic chain.

DOI: 10.1103/PhysRevC.101.064322

I. INTRODUCTION

One of the most interesting phenomena in recent years for the nuclear community is the shape coexistence and shape phase transition in the ground state of atomic nuclei along isotopic chains. Many successful studies have been performed both theoretically, using different models, and experimentally in the near past to study this phenomena.

Covariant density functional theory has been successfully applied to many isotopic chains. Namely, it has been used to study Ru and Mo [1], Kr [2,3], Zr and Sr [3], Pb [4], and Pd, Xe, Ba, Nd, Sm, Gd, and Dy [5]. The obtained results were reasonable and close to experimental data.

In Ref. [6] the author uses relativistic mean-field theory (RMFT) without pairing to calculate the binding energy, the charge quadrupole moment, and the root-mean-square radius of Ge and Zn isotope chains. However, the author does not use constrained calculations and impose axial symmetry, thus he cannot accurately locate the ground state minimum. In fact the author himself suggests the necessity of triaxial calculations. Another similar study was performed in Ref. [7] to study Zn isotopes using RMFT. However, in this study pairing correlations were taken into account by means of BCS theory.

There are many nuclear structure models used to study the nuclear properties and shape transitions such as complete spectroscopy and Coulomb excitation, the interacting boson model (IBM), relativistic and nonrelativistic models using Hartree-Fock-Bogolibov (HFB), and self-consistent Hartree-Fock models [8–18]. In this regard, a realistic description of the structural evolution and shape coexistence in Ge, Se, and Zn isotopes has been addressed earlier in many theoretical studies within different frameworks. Toh *et al.* studied the shape coexistence of Ge and Se with complete spectroscopy and Coulomb excitation, by calculating the means of multiple Coulomb excitation, and used it to determine the properties of nuclear states [19]. Garcia-Ramos and Heyde studied the shape evolution and shape coexistence in Po isotope chains using the interacting boson model with configuration mixing [20]. They obtained the IBM Hamiltonian and calculated excitation energies, $B(E2)$'s, electric quadrupole moments, nuclear radii and isotopic shifts, quadrupole shape invariants, wave functions, and deformations. Their results agree with the experimental data for all the studied observables [21].

Nomura *et al.* [22] studied the shape transitions and shape coexistence in the Ge and Se isotopes within the IBM with the microscopic input from a self-consistent mean-field calculation based on the Gogny-D1M energy density functional. They discussed the potential energy surface, the ground state properties, and the pairing energy for protons and neutrons in Ge and Se isotopes. The Gogny-D1M energy surfaces predict the coexistence between the prolate and oblate shapes in the lightest nuclei in both isotopic chains. For shapes around $N = 40$, coexistence between spherical and γ-soft (i.e., the energy does not change with the value of γ) shapes is observed, When the neutron number increases towards the $N = 50$ shell closure, weakly deformed prolate shapes are obtained. On the other hand, for $52 \leqslant N \leqslant 62$, a number of nuclei exhibiting γ-soft shapes *(which means the nucleus shape changed smoothly in the isotopic chain)* and coexistence between prolate and oblate shapes are observed [22].

*Corresponding author: habusara@birzeit.edu
†physics.sh@gmail.com

He also studied the shape evolution in Kr isotopes using the same models but with input coming from a self-consistent mean-field calculation based on the Gogny energy density functional and relativistic HFB with DD-PC1 and DD-ME2 parametrizations. For neutron-deficient isotopes there is no notable difference between relativistic and collectivistic models. However, they provide different prediction for neutron-rich isotopes [2].

This article is organized as follows. In Sec. II a theoretical framework of the RHB formalism is presented. In Secs. III, IV, and V, the calculations of potential energy surfaces and physical properties are discussed and compared to available experimental data and the results from other models. A summary and conclusions are presented in Sec. VI.

II. THEORETICAL FRAMEWORK

For the present investigation, the self-consistent relativistic Hartree-Bogoluibove (RHB) model with a density-dependent finite-range meson-exchange model and a density-dependent zero-range point-coupling model is used [23–27]. These models provide a very successful and excellent description of different ground states and excited state properties over the entire nucleic chart [24,28–38]. The present investigation uses the very successful, density-dependent point-coupling DD-PC1 [23] and nonlinear meson-nucleon coupling NL3* [39] parameters.

A. The meson-exchange model

The meson-exchange model is defined by the standard Lagrangian density with medium dependence vertices [40]:

$$\begin{aligned}\mathcal{L} &= \overline{\psi}[\gamma(i\partial - g_\omega\omega - g_\rho\vec{\rho}\vec{\tau} - eA) - m - g_\sigma\sigma]\psi \\ &+ \tfrac{1}{2}(\partial\sigma)^2 - \tfrac{1}{2}{m_\sigma}^2\sigma^2 - \tfrac{1}{4}\mathbf{\Omega}_{\mu\nu}\mathbf{\Omega}^{\mu\nu} + \tfrac{1}{2}m_\omega^2\omega^2 \\ &- \tfrac{1}{4}\vec{\mathbf{R}}_{\mu\nu}\vec{\mathbf{R}}^{\mu\nu} + \tfrac{1}{2}m_\rho^2\vec{\rho}^2 - \tfrac{1}{4}\mathbf{F}_{\mu\nu}\mathbf{F}^{\mu\nu}, \end{aligned} \tag{1}$$

where m is the bare nucleon mass and ψ denotes the Dirac spinors. The masses m_σ, m_ω, and m_ρ are those of the σ meson, the ω meson, and the ρ meson, with the corresponding coupling constants for the mesons to the nucleons being g_σ, g_ω, g_ρ, respectively, and e is the charge of the proton. These coupling constants and unknown meson masses are the Lagrangian Eq. (1) parameters. Here, $\Omega^{\mu\nu}$, $\vec{R}^{\mu\nu}$, and $F^{\mu\nu}$ are the field tensors of the vector fields ω, ρ, and the photon.

This linear model was first introduced by Walecka [41,42]; however, this simple model does not provide a quantitative description of a nuclear system [43,44] with interaction terms that are only linear in the meson fields. For a realistic description of complex nuclear system properties one can introduce either a nonlinear self-coupling or a density dependence in the coupling constants.

For the nonlinear self-coupling, one has to add the following term to the Lagrangian:

$$U(\sigma) = \tfrac{1}{2}m_\sigma^2\sigma^2 + \tfrac{1}{3}g_2\sigma^3 + \tfrac{1}{4}g_3\sigma^4; \tag{2}$$

for scalar mesons this has turned out to be crucial [43]. This model has been successfully used in a number of studies [40,45–47]. We have used the recently proposed parameter set NL3* [39], which is a modern version of the widely used parameter set NL3 [46]. It improves the description of the ground state properties of many nuclei over the parameter set NL3 and provides a simultaneously excellent description of excited states with collective character in spherical as well as in deformed nuclei. From the Lagrangian density, one can easily obtain the Hamiltonian density, which for the static case reads

$$\begin{aligned}\mathcal{H} &= \sum_{i=1}^{A}\psi_i^\dagger(\alpha\mathbf{p} + \beta m)\psi_i \\ &+ \frac{1}{2}\big[(\nabla\sigma)^2 + m_\sigma^2\sigma^2\big] - \frac{1}{2}\big[(\nabla\omega)^2 + m_\omega^2\omega^2\big] \\ &- \frac{1}{2}\big[(\nabla\rho)^2 + m_\rho^2\rho^2\big] - \frac{1}{2}(\nabla A)^2 \\ &+ [g_\sigma\rho_s\sigma + g_\omega\vec{j}_\mu\omega^\mu + g_\rho\vec{j}_\mu\cdot\vec{\rho}^\mu + e j_{p\mu}A^\mu]. \end{aligned} \tag{3}$$

We have also introduced the isoscalar-scalar density, the isoscalar-vector current, the isovector-vector current, and the electromagnetic current:

$$\rho_s(r) = \sum_{i=1}^{A}\overline{\psi}_i(r)\psi_i(r), \tag{4}$$

$$j_\mu = \sum_{i=1}^{A}\overline{\psi}_i(r)\gamma_\mu\psi_i(r), \tag{5}$$

$$\vec{j}_\mu = \sum_{i=1}^{A}\overline{\psi}_i(r)\vec{\tau}\psi_i(r), \tag{6}$$

$$\vec{j}_{p\mu} = \sum_{i=1}^{Z}\psi_i^\dagger(r)\gamma_\mu\psi_i(r), \tag{7}$$

where the summation is performed only over occupied orbits in the Fermi sea of positive energy states

B. The point-coupling model

The effective Lagrangian density for the density-dependent point-coupling model [23,48,49] that includes the isoscalar-scalar, isoscalar-vector, and isovector-vector four-fermion interactions is given by

$$\begin{aligned}\mathcal{L} &= \bar{\psi}(i\gamma.\partial - m)\psi \\ &- \frac{1}{2}\alpha_s(\hat{\rho})(\bar{\psi}\psi)(\bar{\psi}\psi) - \frac{1}{2}\alpha_V(\hat{\rho})(\bar{\psi}\gamma^\mu\psi)(\bar{\psi}\gamma_\mu\psi) \\ &- \frac{1}{2}\alpha_{TV}(\hat{\rho})(\bar{\psi}\vec{\tau}\gamma^\mu\psi)(\bar{\psi}\vec{\tau}\gamma_\mu\psi) \\ &- \frac{1}{2}\delta_S(\partial_\nu\bar{\psi}\psi)(\partial^\nu\bar{\psi}\psi) - e\bar{\psi}\gamma\cdot\mathbf{A}\frac{1-\tau_3}{2}\psi. \end{aligned} \tag{8}$$

It contains the free-nucleon Lagrangian and the point-coupling interaction terms, and in addition to these two, the model includes the coupling of the proton to the electromagnetic field. The derivative terms in Eq. (8) account for the leading effects of finite-range interactions that are crucial for a quantitative description of the nuclear properties.

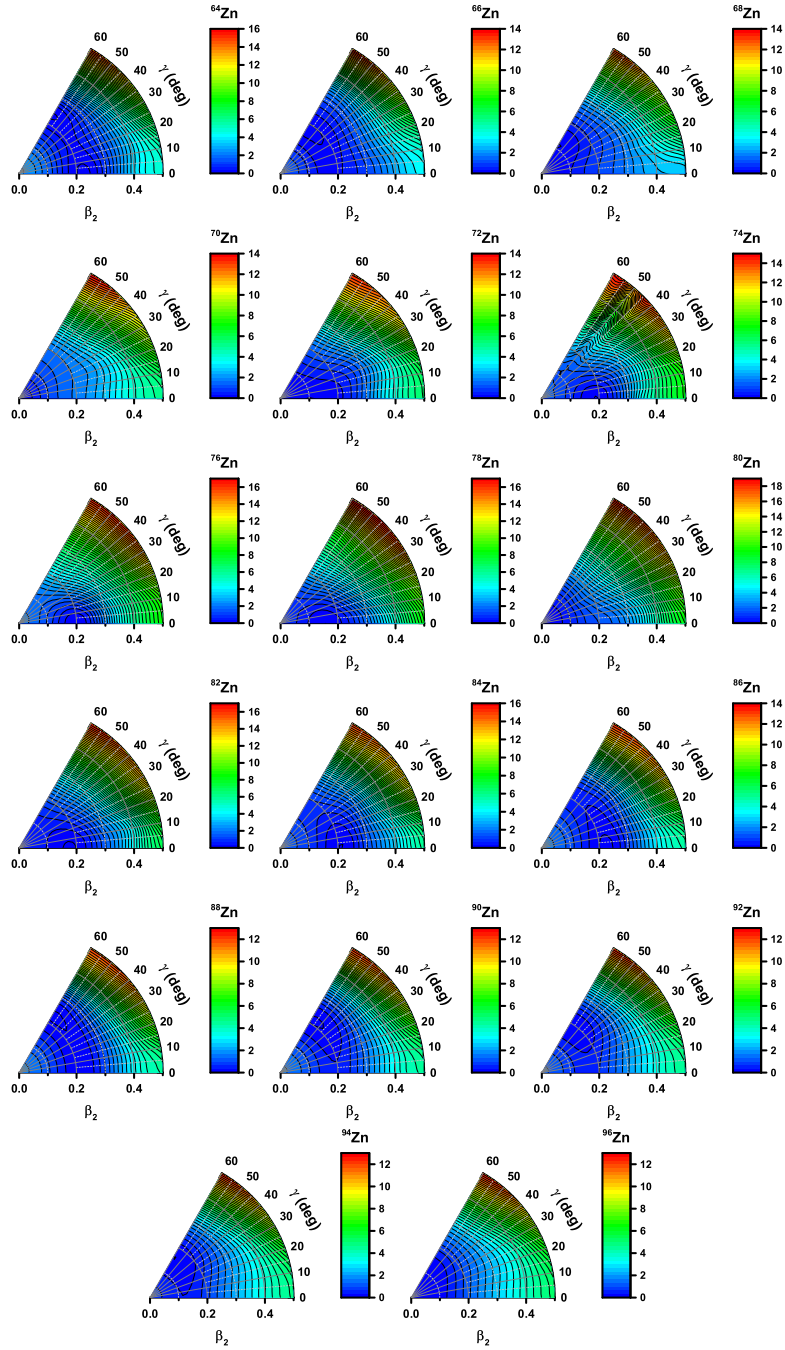

FIG. 1. Potential energy surfaces of even-even Zn isotopes from the neutron number ($34 \leqslant N \leqslant 66$) as functions of the quadrupole deformation, obtained from triaxial RHB calculations with constrained quadrupole deformation. The effective interactions used are NL3*. The surfaces are scaled such that the ground state has a 0 MeV energy.

The Hamiltonian can be written as

$$\mathcal{H} = \sum_{i=1}^{A} \psi_i^\dagger (\alpha \mathbf{p} + \beta m)\psi_i - \frac{1}{2}(\nabla A)^2 + \frac{1}{2} e j_p^\mu A_\mu + \frac{1}{2}\left[\alpha_S \rho_s^2 + \alpha_V j_\mu j^\mu + \alpha_{TV} \vec{j}_\mu \cdot \vec{j}^\mu + \delta_S \rho_s \Box \rho_s\right]. \quad (9)$$

The functional form of the point-couplings chosen is

$$\alpha_i(\rho) = a_i + (b_i + c_i x)e^{-d_i x} \qquad (i = S, V, TV), \quad (10)$$

where $x = \rho/\rho_{\text{sat}}$, and ρ_{sat} denotes the nucleon density at saturation in symmetric nuclear matter. In the present work, we have used the recently developed density-dependent point-coupling interaction DD-PC1 [23].

In the present investigation, the triaxial RHB model with a separable pairing model is used [50,51]. In the presence of pairing the single-particle density matrix is generalized to two

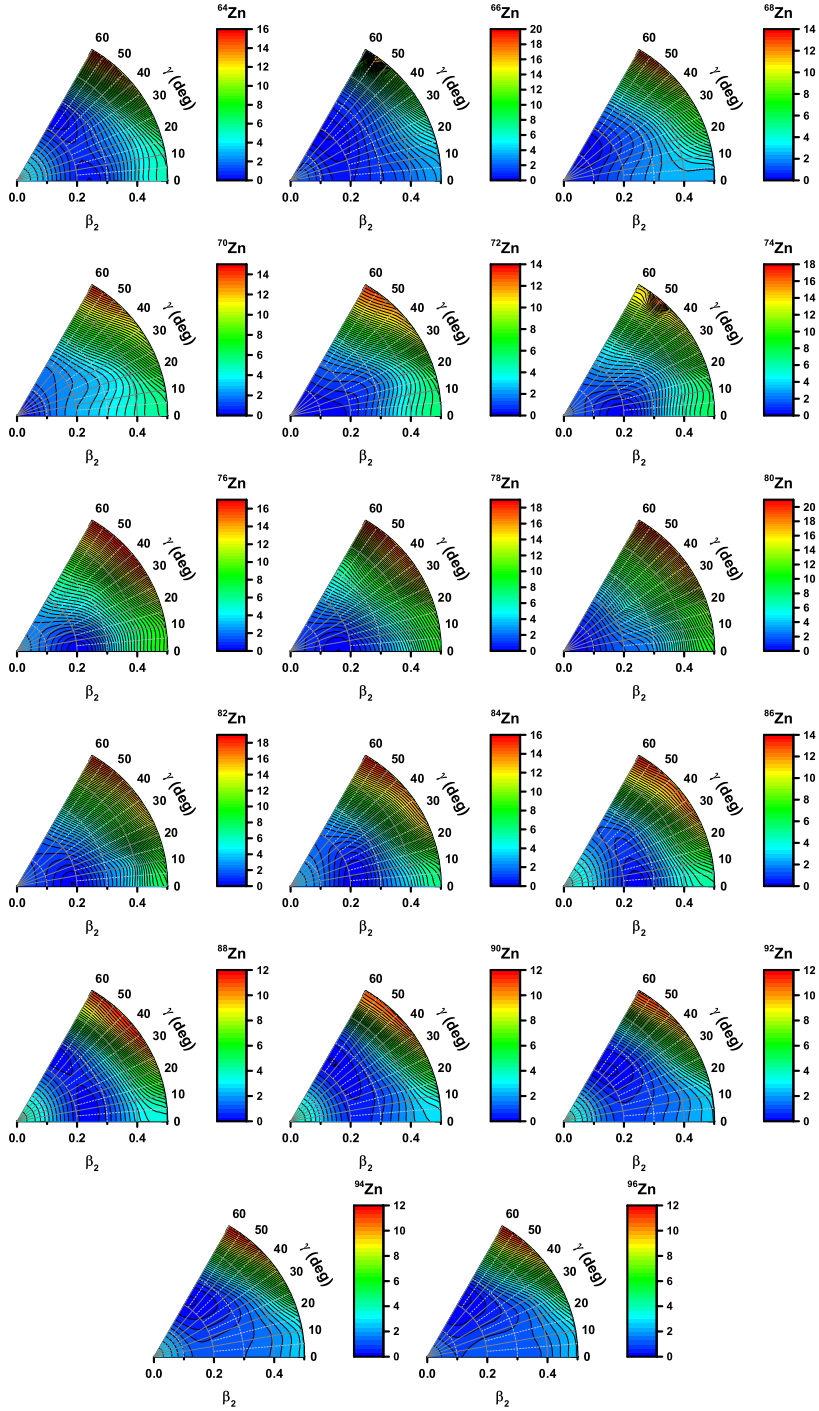

FIG. 2. Similar to Fig. 1, but using the DD-PC1 parametrization.

densities [52]: the normal density $\hat{\rho}$ and the pairing tensor $\hat{k}$. The RHB energy density functional is then given by

$$E_{\mathrm{RHB}}[\hat{\rho},\hat{k}] = E_{\mathrm{RMF}}[\hat{\rho}] + E_{\mathrm{pair}}[\hat{k}], \tag{11}$$

where $E_{\mathrm{RMF}}[\hat{\rho}]$ is given by

$$E_{\mathrm{RMF}}[\psi,\bar{\psi},\sigma,\omega^{\mu},\vec{\rho^{\mu}},A^{\mu}] = \int d^3r\mathcal{H}, \tag{12}$$

and the $E_{\mathrm{pair}}[\hat{k}]$ is given by

$$E_{\mathrm{pair}}[\hat{k}] = \frac{1}{4}\sum_{n_1n_1'}\sum_{n_2n_2'} k^{*}_{n_1n_1'}\langle n_1n_1'|V^{PP}|n_2n_2'\rangle k_{n_2n_2'}. \tag{13}$$

The index n refers to the original basis, and $\langle n_1n_1'|V^{PP}|n_2n_2'\rangle$ are the matrix elements of the two-body pairing interaction. The effective interaction in the pp channel, in **r** space has

TABLE I. Nuclei with two ground state minima for Zn isotopes. Locations of the ground state minima are indicated by (β^0, γ^0). In the second column, NL3* results are shown, while DD-PC1 results are shown in the third column.

Nucleus	NL3*	DD-PC1
^{64}Zn	(0.20, 0° and 0.20, 60°)	(0.25, 60°) and (0.25, 0°)
^{88}Zn	(0.25, 60°)	(0.25, 60°) and (0.25, 0°)

the form

$$V^{PP}(\mathbf{r_1}, \mathbf{r_2}, \mathbf{r_1'}, \mathbf{r_2'}) = -G\delta(\mathbf{R} - \mathbf{R}')P(\mathbf{r})P(\mathbf{r}'), \tag{14}$$

where

$$\begin{aligned} \mathbf{R} &= \frac{1}{\sqrt{2}}(\mathbf{r_1} + \mathbf{r_2}), \\ \mathbf{r} &= \frac{1}{\sqrt{2}}(\mathbf{r_1} - \mathbf{r_2}), \end{aligned} \tag{15}$$

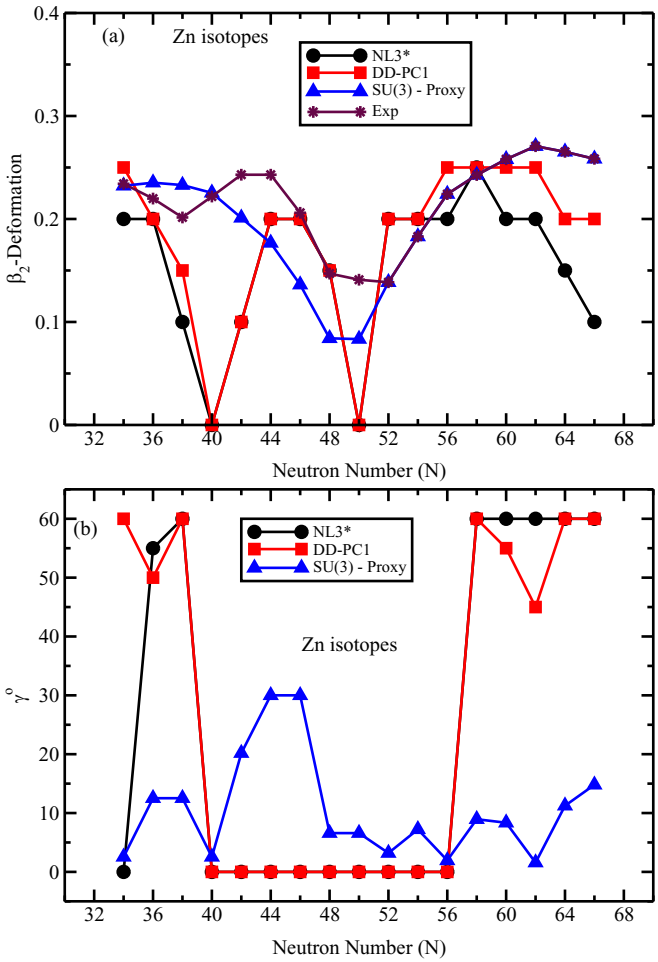

FIG. 3. Quadrupole deformation parameters β_{20} (a) and γ (b) for even-even Zn isotopes using NL3*, DD-PC1, SU(3)-proxy, and experimental data [60] as a function of the neutron number (N).

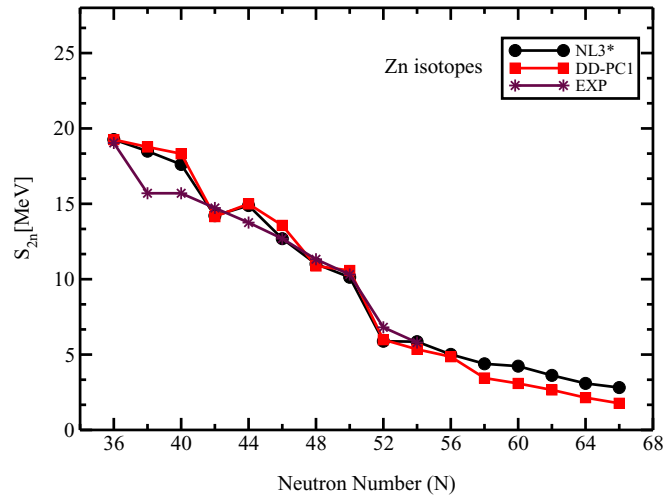

FIG. 4. Two-neutron separation energy for even-even Zn isotopes using NL3* (circles), DD-PC1 (squares), and experimental data [61] (stars) as a function of the neutron number (N).

being the center of mass and the relative coordinates, respectively. The form factor $P(\mathbf{r})$ is of the Gaussian shape:

$$P(\mathbf{r}) = \frac{1}{(4\pi a^2)^{3/2}} e^{-r^2/2a^2}. \tag{16}$$

The two parameters $G = 728$ MeV fm^3 and $a = 0.644$ fm of this interaction are the same for protons and neutrons. It is derived in Refs. [53–56] by a mapping of the $^1S_0$ pairing gap of infinite nuclear matter to that of the Gogny force D1S [57].

C. Numerical details

We perform constrained calculations on the total energy using the triaxial RHB framework, to enable us to locate a global ground state minimum and track the evolution of the ground state shape through the specified isotopic chains. The covariant density functional theory (CDFT) equations are solved on the basis of an isotropic three-dimensional harmonic oscillator in Cartesian coordinates. The truncation of the basis is performed in such a way that all states belonging to the shells up to fermionic $N_F = 14$ and bosonic $N_B = 20$ are taken into account. The constrained calculations are performed by imposing constraints on both axial and triaxial mass quadrupole moments.

The method of quadratic constraints uses an unrestricted variation of the function

$$\langle \hat{H} \rangle + \sum_{\mu=0,2} C_{2\mu}(\langle \hat{Q}_{2\mu} \rangle - q_{2\mu})^2, \tag{17}$$

where $\langle \hat{H} \rangle$ is the total energy, $\langle \hat{Q_{2\mu}} \rangle$ denotes the expectation values of mass quadrupole operators,

$$\hat{Q}_{20} = 2z^2 - x^2 - y^2 \quad \text{and} \quad \hat{Q}_{22} = x^2 - y^2, \tag{18}$$

$q_{2\mu}$ is the constrained value of the multipole moment, and $C_{2\mu}$ is the corresponding stiffness constant [52]. Moreover, the quadratic constraint adds an extra force term, $\sum_{\mu=0,2} \lambda_\mu \hat{Q}_{2\mu}$,

to the system, where

$$\lambda_\mu = 2C_{2\mu}(\langle\hat{Q}_{2\mu}\rangle - q_{2\mu}) \tag{19}$$

for a self-consistent solution. This term is necessary to force the system to a point in deformation space different from a stationary point. The augmented Lagrangian method [58] has also been implemented in order to resolve the problem of convergence of the self-consistent procedure, which diverges while increasing the value of the stiffness constant $C_{2\mu}$ used in the procedure. Using this procedure we can locate the ground state deformation for the even-even nuclei in this study. In performing this calculation, β is taken from 0 to 0.5 in steps of 0.05 and γ is take from 0 to 60 in steps of 5.

In addition, we calculate the value of several physical observables at the ground state deformation. These observables are the following: the two-neutron separation energy, the nucleon radius, and the charge radius.

The two-neutron separation (S_{2n}) is the energy needed to remove two neutrons from a nucleus, and it is given by

$$S_{2n}(N) = BE\left({}^{A}_{Z}X_N\right) - BE\left({}^{A}_{Z}X_{N-2}\right). \tag{20}$$

The nuclear charge radius plays a key role in studying the character of the nucleus and testing theoretical models of nuclei. It is calculated using the proton radius:

$$R_c = \sqrt{R_p^2 + 0.64}, \tag{21}$$

where is 0.64 is related to the finite volume of the proton (volume correction).

For a comprehensive description of the nuclei under consideration and their spectra beyond mean field must be applied, and the calculation of the potential surface energy serves only as the first step. However, this is beyond the scope of the current article.

III. ZN ISOTOPES

A. Triaxial symmetry

Potential energy surfaces for Zn isotopes using both NL3* and DD-PC1 are presented in Figs. 1 and 2, respectively.

The shape coexistence in Zn isotopes is very limited among the even-even isotopes considered in this study. It can be seen from DD-PC1 calculations that the coexistence is only in two nuclei; namely: ^{64,88}Zn, which correspond to neutron numbers 34 and 58, respectively. For NL3*, it predicts the shape coexistence just in ^{64}Zn. Each parametrization predicts a different shape for $N = 34$. While NL3* predicts a prolate shape, DD-PC1 predicts an oblate one. The difference comes from the fact that this nucleus has two competing minima, prolate and oblate as shown in Table I. For each parametrization, the deepest minimum is different. However, the difference in energy between these two minima in both cases is around 0.5 MeV.

For ^{88}Zn, only DD-PC1 predicts a shape coexistence, with two axial minima. One of them is prolate and the other is oblate. Both of the two minima are located around $\beta_2 = 0.20$. However, the oblate minimum is found to be slightly deeper in both nuclei. Most of the deformed Zn isotopes in the middle of the chain are prolate, while the isotopes on either side of the chain are found to be oblate.

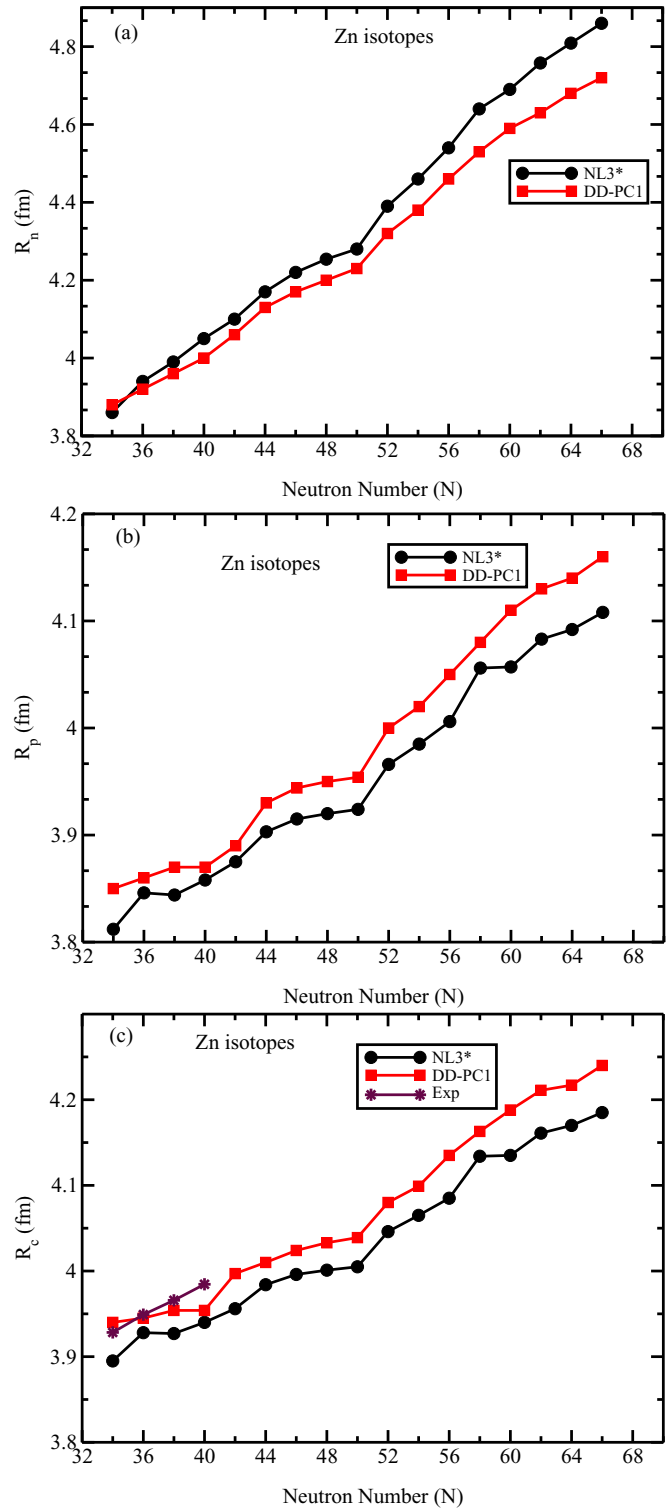

FIG. 5. Neutron (a), proton (b), and charge (c) radii for even-even Zn isotopes in triaxial symmetry using NL3* (circles), DD-PC1 (squares), and experimental data (stars) (experimental data are taken from Ref. [62]) as a function of the neutron number (N).

Locations of the ground state minimum were extracted from the potential energy surfaces (PESs) and plotted in

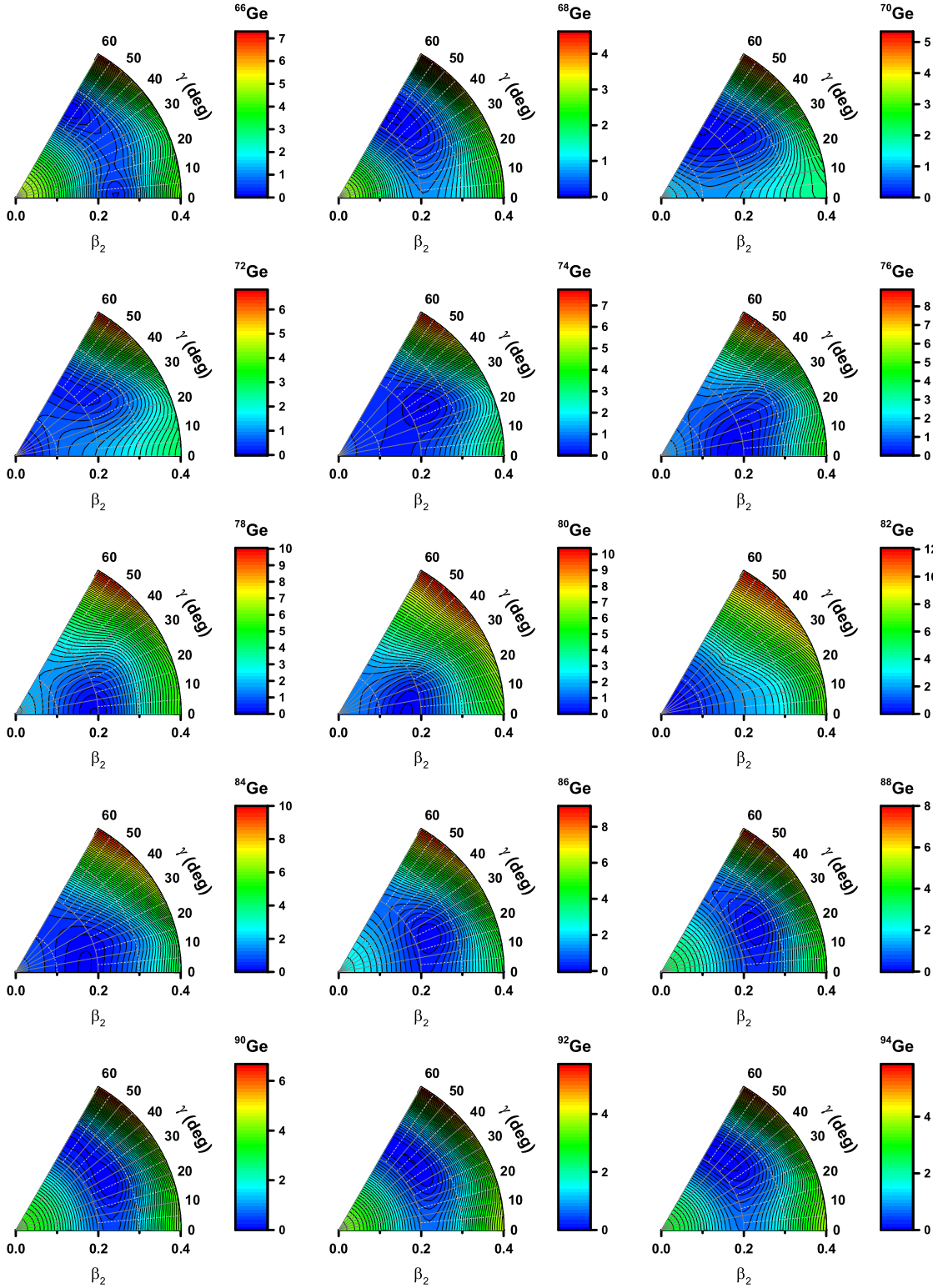

FIG. 6. Potential energy surfaces of even-even Ge isotopes from the neutron number ($34 \leqslant N \leqslant 62$) as functions of the quadrupole deformation, obtained from triaxial RHB calculations with constrained quadrupole deformation. The effective interactions used are NL3*. The surfaces are scaled such that the ground state has a 0 MeV energy.

Fig. 3. It can be seen that results obtained by NL3* and DD-PC1 are in general in agreement with each other. It is worth noting that there are no triaxial minima found in any of our calculations. However, one can argue that for several nuclei there is a softness in the γ deformation, and thus we cannot completely ignore the possibility of a triaxial ground state. This can be clearly seen for ^{68,72,86,90}Zn. It is worth noting that, at both neutron-deficient and neutron-rich sides

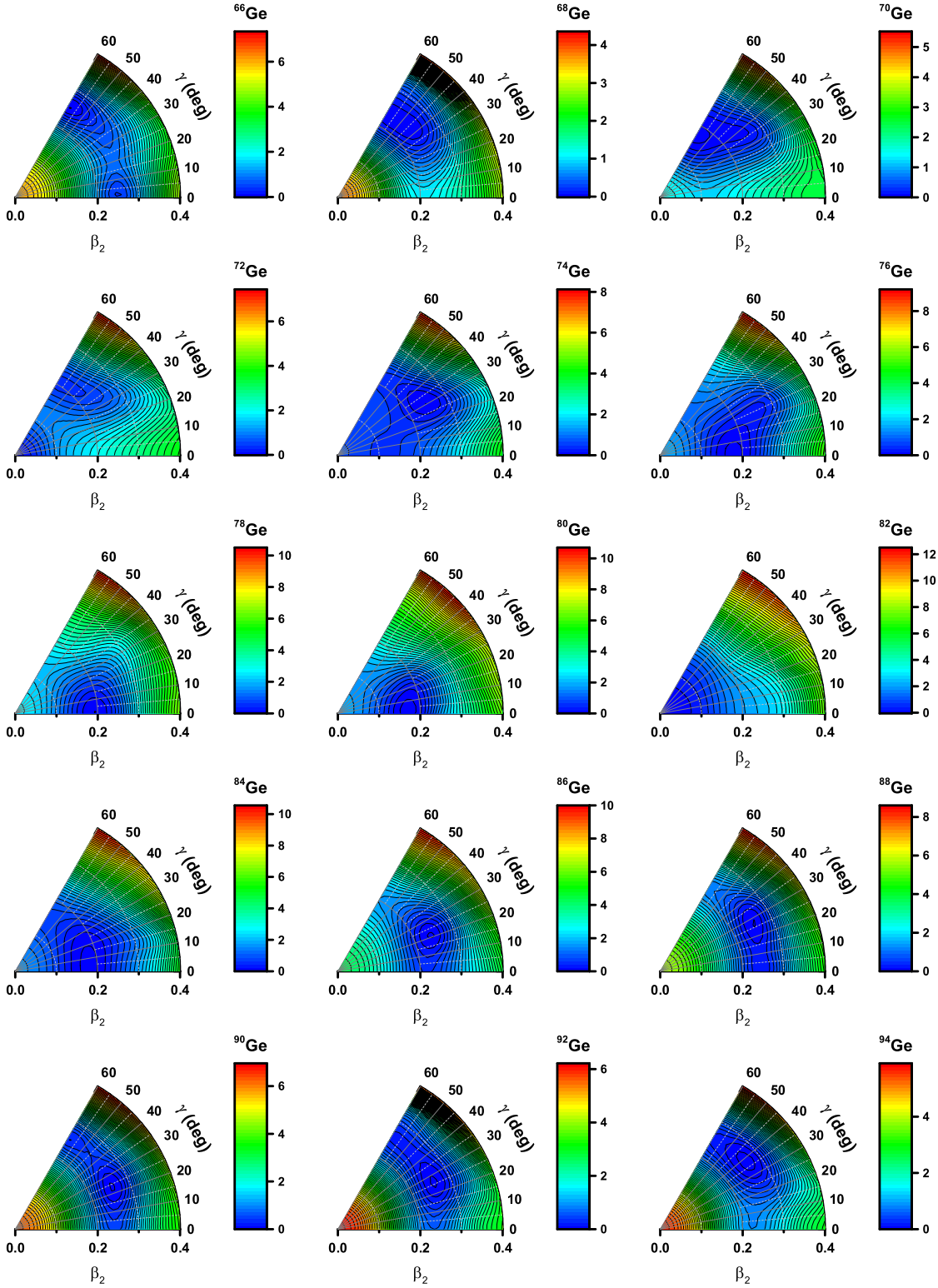

FIG. 7. Similar to Fig. 6, but within the DD-PC1 parametrization.

of the chain, the oblate shape is dominant, while at the middle of the chain the prolate shape is the dominant one. There are several points of shape change: oblate-spherical ($N = 40$), spherical-prolate ($N = 42$), prolate-spherical ($N = 50$), spherical-prolate ($N = 52$), and prolate-oblate ($N = 58$). In all these points of transition we do not find an oblate-prolate transition. All of the transitions go through a spherical shape. These shape transitions lead to the expectation of several sudden changes in the value of the physical observables, as we see later on.

TABLE II. Nuclei with two ground state minima for Ge isotopes. Locations of the two ground state minima are indicated by (β^0, γ^0) for the NL3* parametrization. The first minimum is the deepest minimum.

Nucleus	First minimum (β^0, γ^0)	Second minimum (β^0, γ^0)	ΔE
^{66}Ge	(0.25, 60°)	(0.25, 0°)	0.29
^{72}Ge	(0.00, 0°)	(0.20, 60°)	0.18
^{90}Ge	(0.25, 30°)	(0.25, 60°)	0.09

In Fig. 3 we compare our results with the newly developed SU(3)-proxy [59] and experimental data. Although there are some differences in the values of β_2, all models follow a similar general trend. One of the most interesting features of the SU(3)-proxy model is the shape transition. The authors of Ref. [59] state that if the value of γ is less than 30 then the nucleus has a prolate shape, and if it is greater than 30 then the shape will be oblate. In comparison with the results in Fig. 3, one can see that SU(3)-proxy does not predict an oblate ground state shape; it only predicts spherical and prolate shapes. We can see a perfect agreement in the middle of the isotopic chain, between $N = 40$ and $N = 56$. For $N > 56$, we have total disagreement; our calculations predict an oblate shape while SU(3)-proxy predicts a prolate shape. In the beginning of the chain, the situation is similar; we have an oblate shape while SU(3)-proxy predicts a prolate shape. However, for $N = 34$, our results and those obtained with SU(3)-proxy agree. In addition, we compare our results with experimental data [60]; the results are in good agreement on both sides of the isotopic chain, and difference occurs only at limited points.

In addition, we compute the average deviation between NL3*, DD-PC1, and SU(3)-proxy with the experimental data for β deformation. In all three cases the average deviation is about 0.05. This number is the same as the step size for the calculations mentioned previously. Thus our results are in good agreement with both experimental data and SU(3)-proxy.

B. Physical properties

1. Two-neutron separation energy

In Fig. 4, the two-neutron separation energy is plotted as a function of the neutron number. At a first glance, we see that S_{2n} decreases smoothly as the number of neutrons increases in the Zn isotopic chain. A sudden change appears at neutron magic number $N = 50$ in both NL3* and DD-PC1 calculations. In energy terminology one can claim that the energy necessary to remove two neutrons from a nucleus

TABLE III. Same as Table II, but using the DD-PC1 parametrization. The first minimum is the deepest minimum.

Nucleus	First minimum (β^0, γ^0)	Second minimum (β^0, γ^0)	ΔE
^{66}Ge	(0.25, 60°)	(0.25, 0°)	0.42
^{72}Ge	(0.00, 0°)	(0.20, 60°)	0.37
^{90}Ge	(0.25, 30°)	(0.25, 60°)	0.08

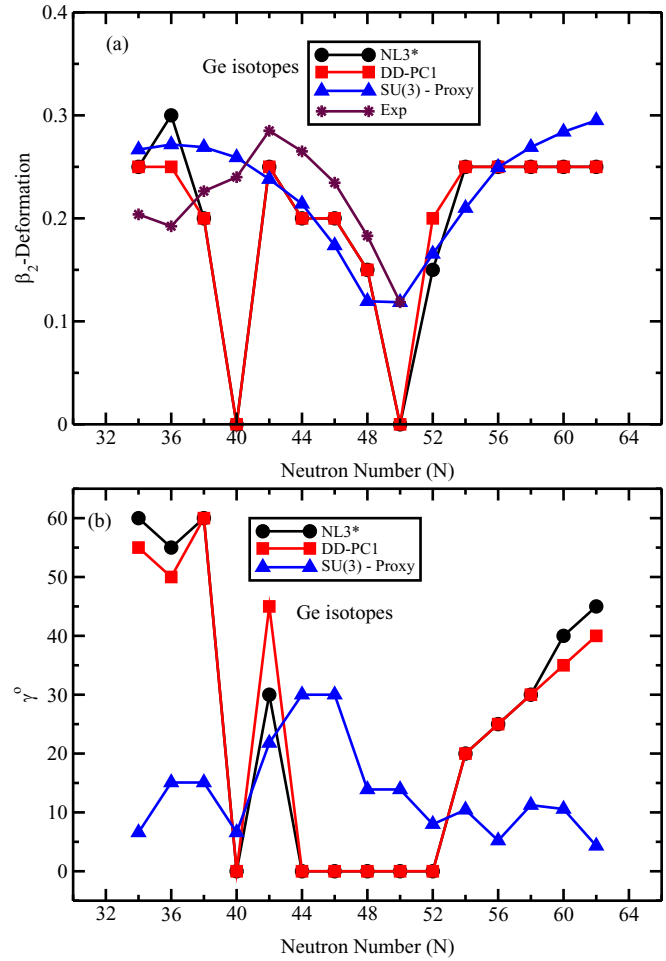

FIG. 8. Similar to Fig. 3, but for Ge isotopes.

(Z, N_{magic}) is much higher than that needed to remove two neutrons from the nucleus $(Z, N_{\text{magic}+2})$, which breaks the regular trend. In addition, an abrupt decrease in S_{2n} at $N = 42$ is observed. This sudden change is referred to as the shape transition of the ground state from spherical at $N = 40$ to prolate at $N = 42$. Also one can notice at the low neutron side of the chain there is a bit of disagreement between our results and the experimental one. For $N = 40$ the reason for discrepancy is due to different predictions between CDFT and experimental data; CDFT predicts a spherical shape but experimental data predicts deformed shape. However, as we move along the chain this discrepancy disappears.

The average deviation between our calculations and experimental data is found to be around 2 MeV. This deviation lies within the acceptable errors for CDFT predictions.

2. Neutron, proton, and charge radii

In Fig. 5(a), the neutron radius changes smoothly with the neutron number N. However, NL3* and DD-PC1 show sudden changes in the neutron radius that can be explained by the change in shape and the fact that $N = 50$ is a magic number. Figures 5(b) and 5(c) show the proton and charge radii, respectively. One can see several sudden changes in

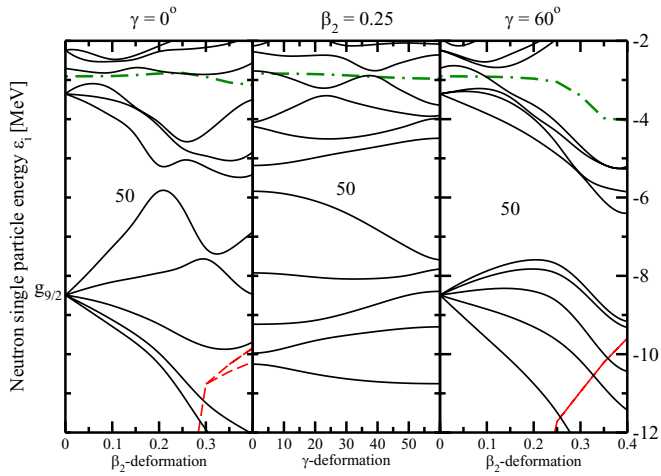

FIG. 9. Single-neutron energy levels of ^{90}Ge as a function of β_2 deformation. Solid (black) curves correspond to levels with positive parity, and (red) dashed curves denote levels with negative parity. The dot-dashed (green) curves correspond to the Fermi levels. The panels on the left and the right display prolate ($\gamma = 0°$) and oblate ($\gamma = 60°$) axially symmetric single-particle levels, respectively. In the middle panel of the figure, neutron levels are plotted as functions of γ for a fixed value of the axial deformation $|\beta_2|$ at the approximate position of the mean-field minimum.

the proton radius located at $N = 42$, 50, and 58, which can be attributed to the points of shape change mentioned in the previous part. In the proton subsystem the sudden change in the radius is strongly affected by the changing ground state deformation contrary to the neutron subsystem. Good agreement with experimental data is found.

IV. GE ISOTOPES

A. Triaxial symmetry

Figures 6 and 7 display PESs of the even-even $^{66-94}$Ge isotopes for NL3* and DD-PC1 parametrizations, respectively.

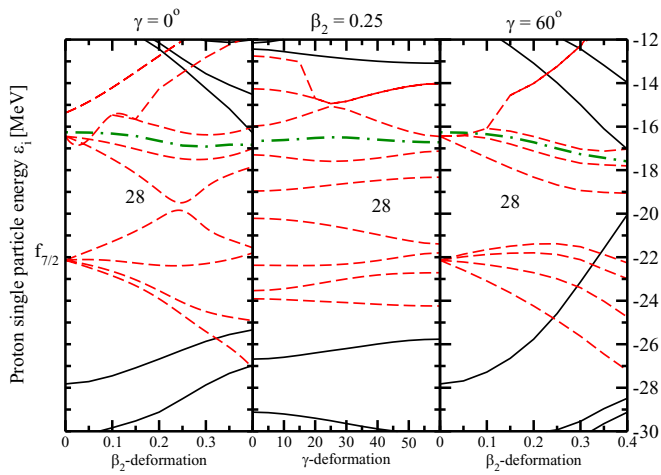

FIG. 10. Similar to Fig. 9 but for protons.

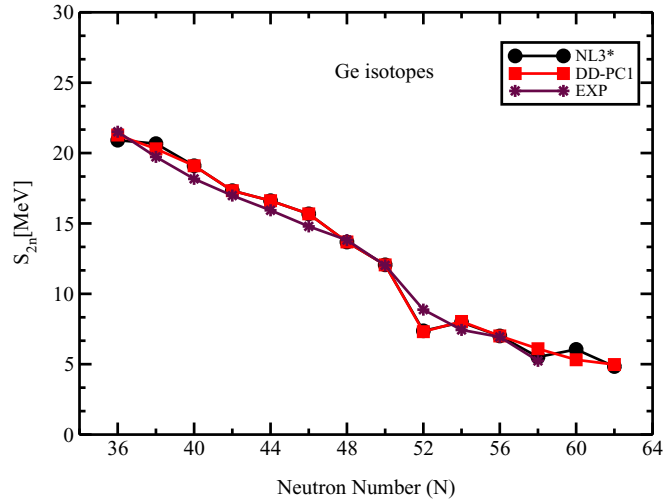

FIG. 11. Two-neutron separation energy for even-even Ge isotopes using NL3* (circles), DD-PC1 (squares), and experimental data [61] (stars) as a function of the neutron number (N).

Nuclei that possess two ground state minima are listed in Tables II and III; these nuclei are ^{66,72,90}Ge. Both NL3* and DD-PC1 predict the same two minima for these nuclei. We can see that results obtained from both parametrizations are very close.

The remaining nuclei has only one minimum. The shape of the ground state in ^{68,70}Ge becomes oblate. Thus we have an oblate-spherical shape transition from $N = 38$ to $N = 40$. With the addition of two more neutrons, $N = 42$, ^{74}Ge has a triaxial ground state at $\beta = 0.25$ and $\gamma = 30$ and also has a shape transition from spherical to triaxial. For ^{76,78,80,84}Ge the minimum is a prolate and the value of β_2 decreases from 0.2 to 0.15, leading to a spherical shape for ^{82}Ge. Also in $^{86-94}$Ge there is a triaxial minimum with $\beta = 0.25$.

In Fig. 8 our results are compared with the SU(3)-proxy predictions and experimental data. The predicted γ values are identical in the middle of the isotopic chain from $N = 44$ to $N = 56$. The disagreement in the ground state shape, as in the Zn case, is found to be in the beginning and at the end of the isotopic chain. The most obvious point is that SU(3)-proxy does not predict any oblate shape in the ground state, but predicts a triaxial shape at $N = 44$ and 46.

Thus our results are in good agreement with both experimental data [60] and SU(3)-proxy, where the average deviation is found to be 0.05.

It is interesting to look at one specific case, which is $N = 40$. This nucleus has two ground state minima, and the deepest one as mentioned previously is spherical. This is causing a difference as compared with experimental data. However, this difference is due to shape coexistence for ^{72}Ge. The second minimum has a deformation of $\beta_2 = 0.2$, and that is very close to the experimental value with less than 0.50 MeV higher than the spherical minimum.

The occupation of the single-particle states and the density of states near the Fermi level play an important role in the determining of the nuclear ground state deformation. To understand this role we plotted the single-particle energy level

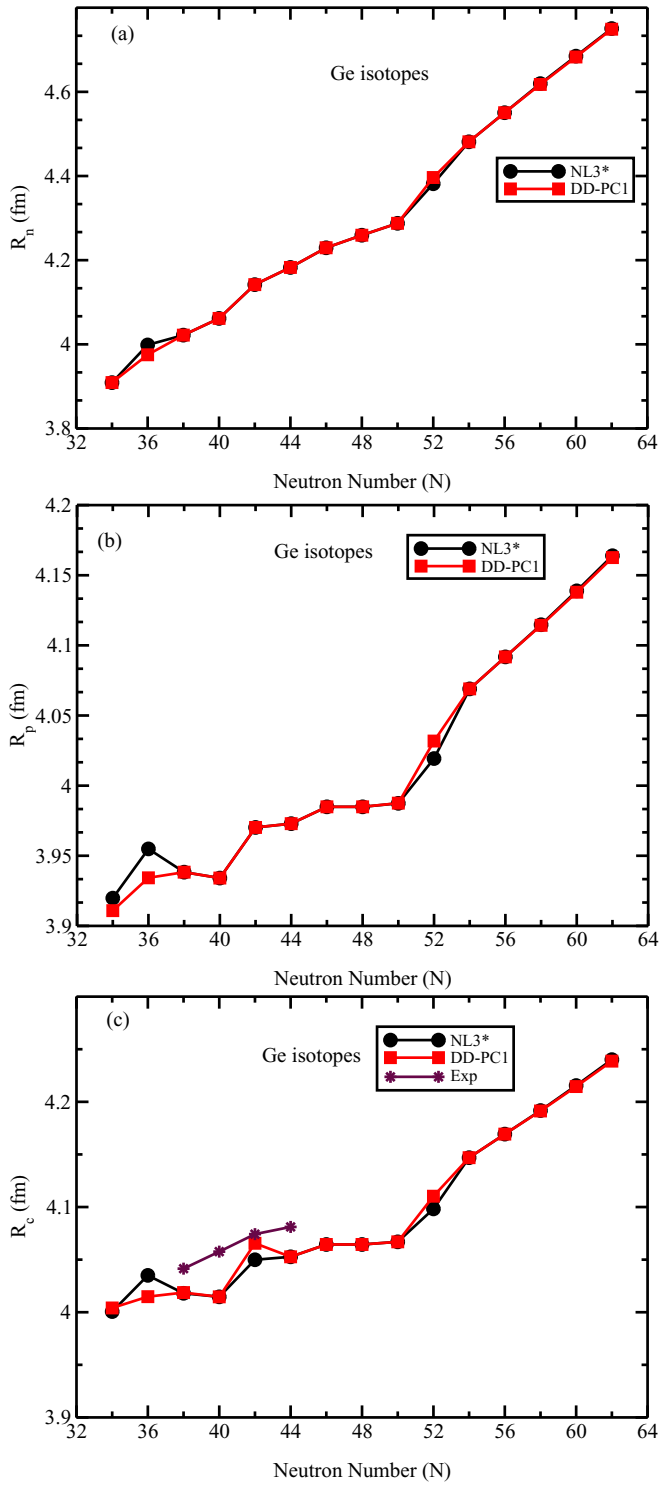

FIG. 12. Similar to Fig. 5, but for Ge isotopes.

of ^{90}Ge for neutron and proton subsystems in Figs. 9 and 10, respectively. One can see in both figures that the magic number shell gap is more pronounced in the oblate case than in the prolate case ($N = 50$, $Z = 28$). In addition, the density of states near the Fermi level for the oblate case is higher than that for the prolate case. One can also notice that the density of states in the middle panel that corresponds to $\beta_2 = 0.25$ is higher in the vicinity of $\gamma = 30$.

Thus one can conclude that the density of states plays an important role in determining the ground state deformation. This feature is very similar to the one seen in the calculations of the fission barrier height. In Fig. 10 of Ref. [63], the authors showed that the height of the fission barrier is reduced due to triaxiality and that was connected to higher density of states for triaxial solution. It was also mentioned in an earlier article by Strutinsky [64].

B. Physical properties

1. Two-neutron separation energy

The two-neutron septation energy is plotted as a function of the neutron number (N) in Fig. 11. One can notice a smooth change in S_{2n} with N, except for $N = 52$, where we can see a sharp change in S_{2n}, and this sharp jump can be attributed to two factors. The first one is due to the magic number $N = 50$, which as we know separation energy increases near magic numbers. The second factor is the sudden change in the ground state shape from prolate in ^{76,78,80}Ge ($N = 46$, 48, 50) to spherical in ^{82}Ge ($N = 52$). There is good agreement between our calculations and the results that were obtained in experiments [61]; the average deviation between our results and experimental data is about 0.50 MeV.

2. Neutron, proton, and charge radii

Figures 12(a) and 12(b) show the radii of neutrons and protons obtained from NL3* and DD-PC1 parametrizations are in agreement with each other with small deviations. One can notice a sharp change in both the neutron radius (R_n) and the proton radius (R_p) at $N = 52$. This sharp change can be attributed to the sudden transition from a spherical shape in ^{82}Ge ($N = 50$) to a deformed shape in ^{84}Ge ($N = 52$). NL3* predicts larger values of R_p compared with the ones obtained using DD-PC1 at $N = 36$. This difference comes from the different locations of the ground state minima. This ground state has axial minima with $\beta = 0.3$ in NL3*, whereas DD-PC1 predicts it to have triaxial minima with $\beta = 0.25$. To verify this, we can notice there is no significant difference between the radii of neutrons and protons obtained from NL3* and DD-PC1 at $N = 34$, which is because the prediction of the ground state minima are the same in NL3* and DD-PC1 parametrizations.

Figure 12(c) shows the charge radius for Ge isotopes; it has behavior identical to that of the proton radius discussed in the previous paragraph.

V. SE ISOTOPES

A. Triaxial symmetry

Figures 13 and 14 display the potential energy surfaces for even-even $^{68-96}$Se using both NL3* and DD-PC1 parametrizations, respectively.

Tables IV and V list all the nuclei that have shape coexistence, which are $^{68,70,74,86-96}$Se. It can be seen that NL3* predicts an oblate minimum to be the deepest one, and the

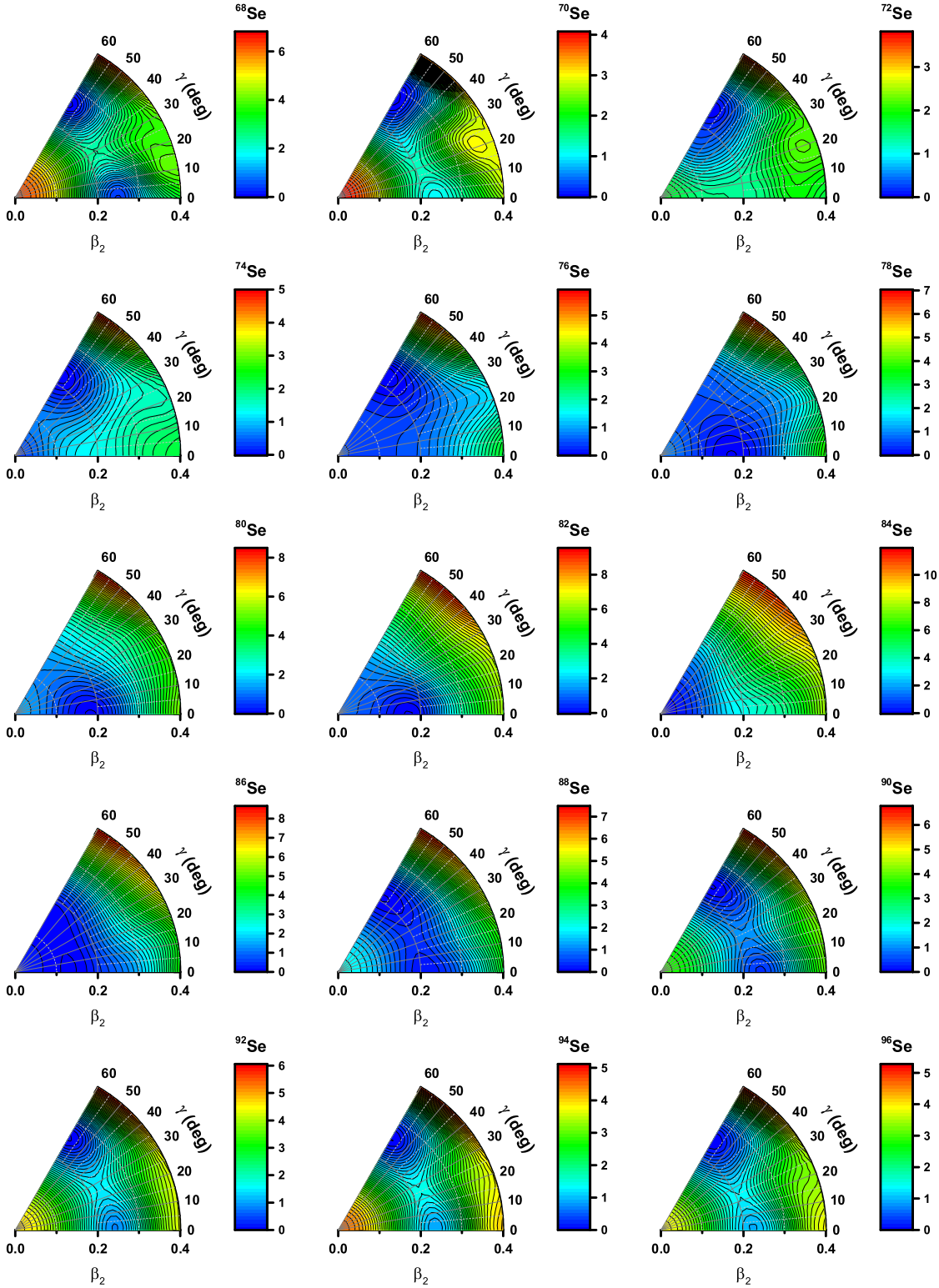

FIG. 13. Similar to Fig. 6, but for Se isotopes using NL3*.

second minimum is a prolate minimum except for ^{74}Se, which has a spherical second minimum. The results obtained from DD-PC1 are in agreement with those from NL3* calculations within one major difference in ^{88,90}Se, where the deepest minimum is a prolate shape and the second minimum is an oblate shape. However, the difference in energy between these minima, both for NL3* and DD-PC1, is less than 400 KeV.

Finally, the ground state has one minimum in ^{72,76,78,80,82,84}Se. This minimum is a prolate shape at $\beta = 0.25$ in ^{72}Se, and it is an oblate shape in ^{76,78,80,82,86}Se with

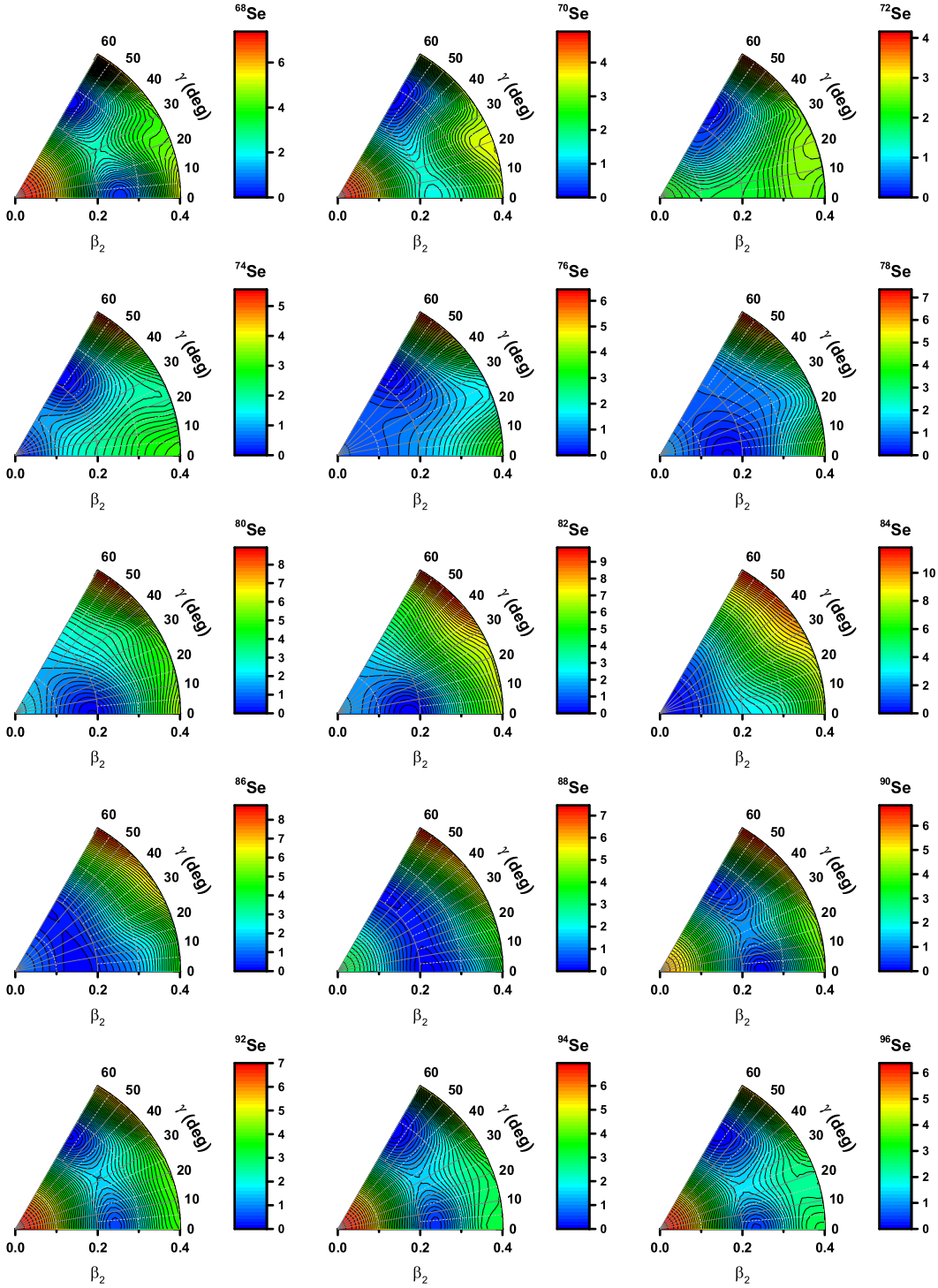

FIG. 14. Similar to Fig. 13, but using the DD-PC1 parametrization.

different values of β varying from 0.15 to 0.2. In ^{84}Se the shape of the ground state changes suddenly to spherical.

In Fig. 15, as expected, we get a good agreement with the SU(3)-proxy model in the middle of the isotopic chain and total disagreement on both sides of the chain. However, here we have a very interesting case. On the neutron-rich side of the chain, shape coexistence is present. If one takes the second minimum into consideration, we notice that the results are in full agreement with the SU(3)-proxy predictions. In addition, we compare our results with experimental data [60]; the results are in good agreement along the chain, and the average deviation is about 0.05.

Similar to ^{90}Ge, we plot single-particle states for ^{90}Se for neutron and proton subsystems in Figs. 16 and 17,

TABLE IV. Nuclei with two ground state minima for Se isotopes. Locations of the two ground state minima are indicated by (β^0, γ^0) for the NL3* parametrization. The first minimum is the deepest minimum.

Nucleus	First minimum (β^0, γ^0)	Second minimum (β^0, γ^0)	ΔE
^{68}Se	(0.25, 60°)	(0.25, 0°)	0.37
^{70}Se	(0.30, 60°)	(0.25, 0°)	1.07
^{74}Se	(0.20, 60°)	(0.00, 0°)	0.27
^{86}Se	(0.15, 0°)	(0.15, 60°)	0.15
^{88}Se	(0.2, 60°)	(0.2, 0°)	0.18
^{90}Se	(0.25, 60°)	(0.25, 0°)	0.38
^{92}Se	(0.25, 60°)	(0.25, 0°)	0.87
^{94}Se	(0.25, 60°)	(0.25, 0°)	0.92
^{96}Se	(0.25, 60°)	(0.25, 0°)	1.10

respectively. ^{90}Se has two minima with an energy difference of 0.38 MeV. The deepest minimum is the oblate shape that corresponds to $\gamma = 60$. We see that in the vicinity of the Fermi level that, for $\gamma = 60$, the density of states are higher than for $\gamma = 0$, in both proton and neutron subsystems. In addition one can notice that the $N = 50$ shell gap and $Z = 28$ are larger for the oblate shape than for the prolate shape. Thus one would expect the prolate minimum to be deeper as shown by our results. For the neutron subsystem the states near the Fermi level drive the deformation up, but in the proton subsystem the state just below the Fermi level does not effect the deformation.

B. Physical properties

1. Two-neutron separation energy

One can see in Fig. 18 that the two-neutron separation energies (S_{2n}) for Se isotopes obtained from NL3* and DD-PC1 are in agreement with each other. There is a sharp change in S_{2n} at $N = 52$ that can be attributed to two factors. The first one is due to the magic number $N = 50$, because we know that separation energy increases as it nears magic numbers. The second factor is the sudden change in the ground state shape from a spherical shape at $N = 50$ to a deformed shape at $N = 52$. The average deviation between our results and experimental data is about 0.70 MeV. Thus, our calculations are in agreement with experimental data [61] except at $N = 52$.

TABLE V. Same as Table IV, but using the DD-PC1 parametrization.

Nucleus	First minimum (β^0, γ^0)	Second minimum (β^0, γ^0)	ΔE
^{68}Se	(0.25, 60°)	(0.25, 0°)	0.33
^{70}Se	(0.30, 60°)	(0.25, 0°)	1.42
^{74}Se	(0.25, 60°)	(0.00, 0°)	0.08
^{86}Se	(0.15, 0°)	(0.15, 60°)	0.19
^{88}Se	(0.2, 0°)	(0.20, 60°)	0.14
^{90}Se	(0.25, 0°)	(0.25, 60°)	0.24
^{92}Se	(0.25, 60°)	(0.25, 0°)	0.55
^{94}Se	(0.30, 60°)	(0.25, 0°)	0.40
^{96}Se	(0.25, 60°)	(0.25, 0°)	0.01

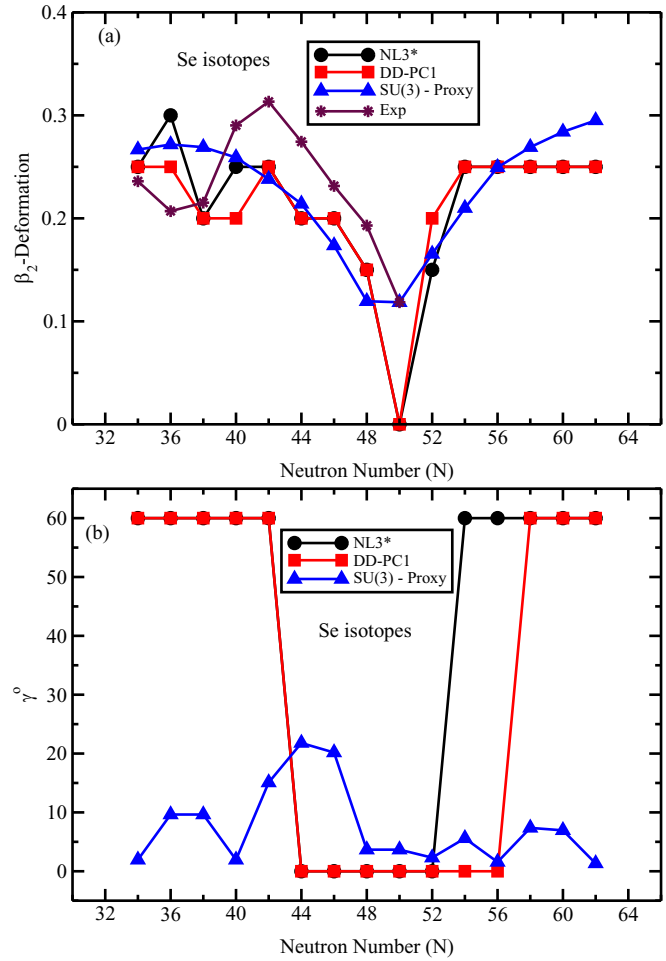

FIG. 15. Similar to Fig. 3, but for Se isotopes.

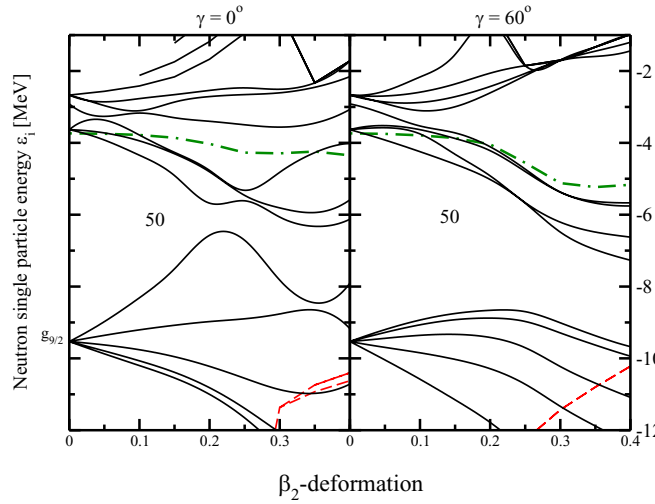

FIG. 16. Single-neutron energy levels of ^{90}Se as a function of β_2 deformation. Solid (black) curves correspond to levels with positive parity, and (red) dashed curves denote levels with negative parity. The dot-dashed (green) curves correspond to the Fermi levels.

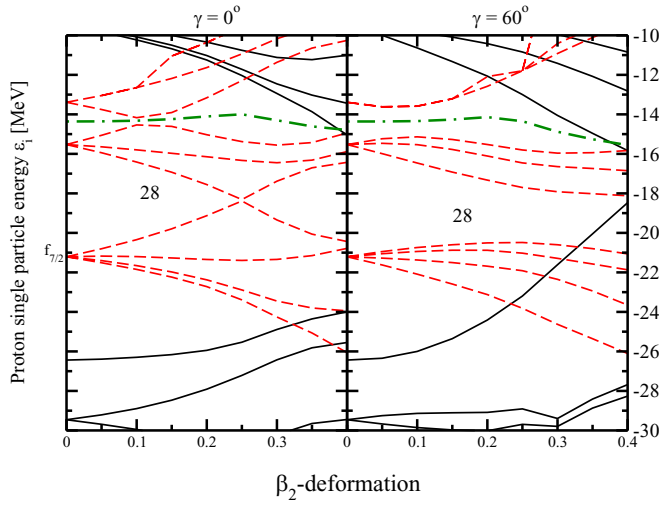

FIG. 17. Similar to Fig. 16, but for protons.

2. *Neutron, proton, and charge radii*

There is good agreement in Figs. 19(a) and 19(b) for the radii of both neutrons and protons obtained from NL3* and DD-PC1 parametrizations. However, there is small deviation when the NL3* results show a higher value of neutron radius. On the other hand, the DD-PC1 results shows a higher value of proton radius. This difference is attributed to the differences in shape evolution for the ground state between NL3* and DD-PC1.

Figure 19(c) shows the charge radii for Se isotopes. One can see that there is a sharp change in the R_c at $N = 52$. This sharp change is attributed to a sudden change of ground state shape from prolate at $N = 50$ to spherical at $N = 52$. Also as we know that the charge radius increases at magic numbers, and $N = 50$ is a magic number. Good agreement with experimental data is found.

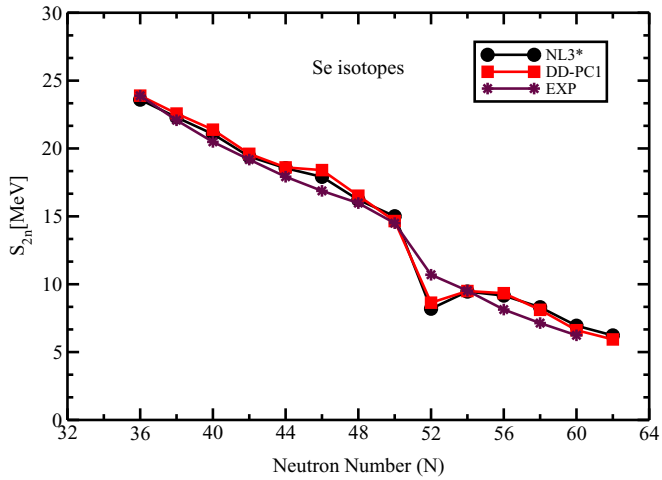

FIG. 18. Two-separation energy for even-even Se isotopes using NL3* (circles), DD-PC1 (squares), and experimental data [61] (up triangle) as a function of the neutron number (N).

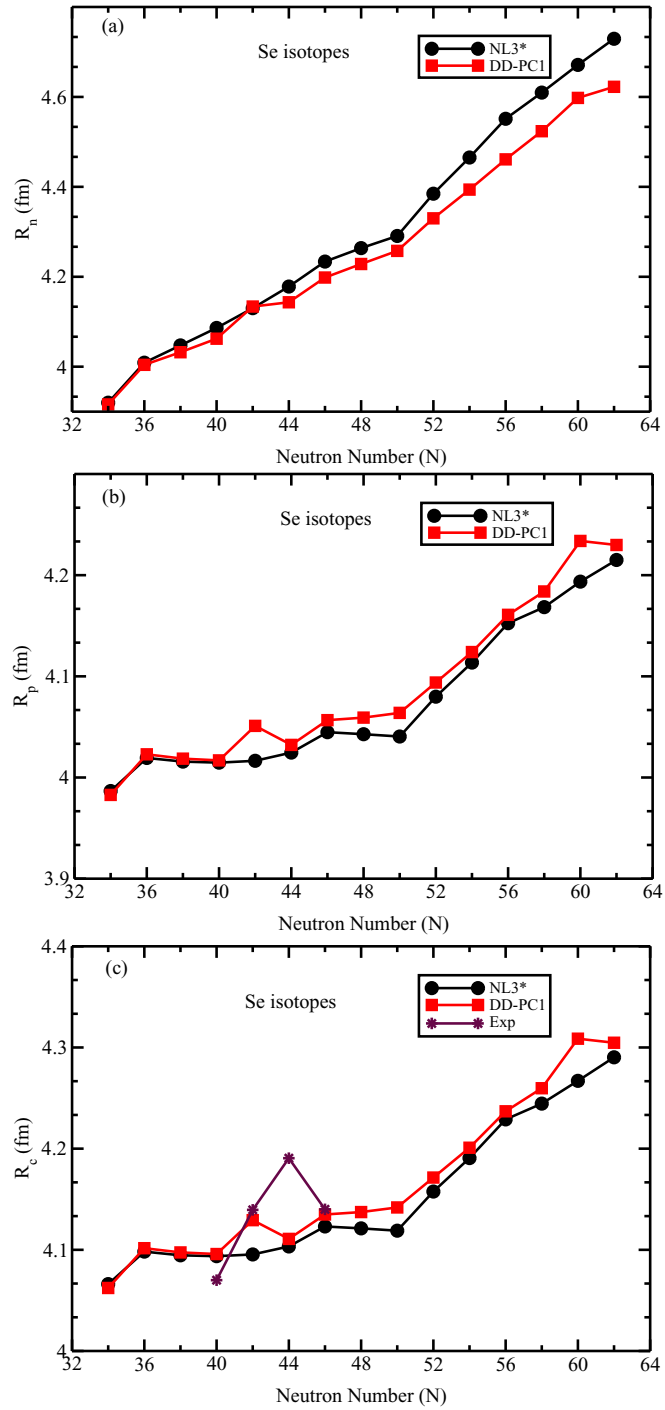

FIG. 19. Similar to Fig. 5, but for Se isotopes.

VI. CONCLUSION

In this article, the relativistic Hartree-Bogoluibove model has been successfully applied to investigate the shape coexistence and physical properties such as two-neutron separation energy and neutron and proton radii in the ground state of Zn ($Z = 30$, $34 \leqslant N \leqslant 64$) isotopes, Ge ($Z = 32$, $34 \leqslant N \leqslant 62$) isotopes, and Se ($Z = 34$, $34 \leqslant N \leqslant 62$) isotopes.

The functional DD-PC1 was adjusted exclusively to the experimental masses of a set of 64 deformed nuclei in the

mass regions $A \approx 150$–180 and $A \approx 230$–250. NL3* was fitted to 12 spherical nuclei. Thus the study of transitional nuclei can be considered as an extrapolation of these two parametrizations and serves as a test of the universality of CDFT parametrizations. The good agreement with experiment, in both two-neutron separation energy and ground state deformation, is a great success of CDFT and is a big step to support the usage of universal energy density functionals in the study of nuclear structure.

Shape coexistence was present in the Ge and Se isotopes and not in the Zn isotopes. No shape coexistence was observed in the Zn isotopes, and all of the minima were in general axial. Several shape transitions from prolate to oblate occur through the chain, but they always pass through the spherical shape. A very good agreement was found when our results were compared with the prediction of SU(3)-proxy, especially in the middle of each isotopic chain. One has to note that SU(3)-proxy is an approximate, analytic treatment of the Nilsson model. It is a good approximation to the full set of orbits in a major shell. It works best for nuclei where microscopic calculations are found to be challenging.

One can see that the smooth change in the ground state deformation is connected with a smooth evolution of the physical properties in the ground state. The sharp jump in most of the physical properties is observed at $N = 50$. This sharp jump is due to the change of the ground state shape in the neighboring nuclei. The density of states near the Fermi level plays a major factor in determining the ground state deformation and the possibility of shape coexistence.

[1] H. Abusara, S. Ahmad, and S. Othman, Phys. Rev. C **95**, 054302 (2017).
[2] K. Nomura, R. Rodríguez-Guzmán, Y. M. Humadi, L. M. Robledo, and H. Abusara, Phys. Rev. C **96**, 034310 (2017).
[3] H. Abusara and S. Ahmad, Phys. Rev. C **96**, 064303 (2017)
[4] T. Naz, S. Ahmad, and H. Abusara, Acta Phys. Pol., B **49**, 1653 (2018).
[5] T. Naz, G. H. Bhat, S. Jehangir, S. Ahmad, and J. A. Sheikh, Nucl. Phys. A. **979**, 1 (2018).
[6] G. Gangopadhyay, Phys. Rev. C **59**, 2541 (1999).
[7] T. T. Wang *et al.*, Eur. Phys. J. A **25**, 29 (2005).
[8] C. A. Grossmann, M. A. LaBonte, G. E. Mitchell, J. D. Shriner, J. F. Shriner, G. A. Vavrina, and P. M. Wallace, Phys. Rev. C **62**, 024323 (2000).
[9] W. Frank, P. von Brentano, A. Gelberg, and H. Harter, Phys. Rev. C **38**, 2358 (1988).
[10] S. Kuyucak, I. Morrison, and T. Sebe, Phys. Rev. C **43**, 1187 (1991).
[11] P. G. Reinhard, D. J. Dean, W. Nazarewicz, J. Dobaczewski, J. A. Maruhn, and M. R. Strayer, Phys. Rev. C **60**, 014316 (1999).
[12] S. Suchyta, S. N. Liddick, Y. Tsunoda, T. Otsuka, M. B. Bennett, A. Chemey *et al.*, Phys. Rev. C **89**, 021301(R) (2014).
[13] E. S. Paul, D. B. Fossan, Y. Liang, R. Ma, and N. Xu, Phys. Rev. C **40**, 1255 (1989).
[14] M. O. Kortelahti, E. F. Zganjar *et al.*, Phys. Rev. C **43**, 484 (1991).
[15] J. L. Egido, L. M. Robledo, and R. R. Rodriguez-Guzman, Phys. Rev. Lett. **93**, 082502 (2004).
[16] M. S. Kaplan, J. X. Saladin, D. F. Winchell, H. Takai, and J. Dudek, Phys. Rev. C **44**, 668 (1991).
[17] G. Lhersonneau *et al.*, Phys. Rev. C **56**, 2445 (1997).
[18] Y. Liang *et al.*, Phys. Rev. C **45**, 1041 (1992).
[19] Y. Toh *et al.*, J. Nucl. Sci. Technol. **39**, 497 (2002).
[20] J. E. Garcia-Ramos and K. Heyde, Phys. Rev. C **92**, 034309 (2015).
[21] J. E. Garcia-Ramos, K. Heyde, L. M. Robledo, and R. R. Rodriguez-Guzman, Phys. Rev. C **89**, 034313 (2014).
[22] K. Nomura, R. Rodriguez-Guzman, and L. M. Robledo, Phys. Rev. C **95**, 064310 (2017).
[23] T. Nikšić, D. Vretenar, and P. Ring, Phys. Rev. C **78**, 034318 (2008).
[24] G. A. Lalazissis, T. Nikšić, D. Vretenar, and P. Ring, Phys. Rev. C **71**, 024312 (2005).
[25] T. Nikšić, D. Vretenar, P. Finelli, and P. Ring, Phys. Rev. C **66**, 024306 (2002).
[26] X. Roca-Maza, X. Viñas, M. Centelles, P. Ring, and P. Schuck, Phys. Rev. C **84**, 054309 (2011).
[27] N. Paar, D. Vretenar, E. Khan, and G. Coló, Rep. Prog. Phys. **70**, 691 (2007).
[28] S. E. Agbemava, A. V. Afanasjev, D. Ray, and P. Ring, Phys. Rev. C **89**, 054320 (2014).
[29] S. E. Agbemava, A. V. Afanasjev, D. Ray, and P. Ring, Phys. Rev. C **95**, 054324 (2017).
[30] A. V. Afanasjev and S. E. Agbemava, Phys. Rev. C **93**, 054310 (2016).
[31] S. E. Agbemava, A. V. Afanasjev, T. Nakatsukasa, and P. Ring, Phys. Rev. C **92**, 054310 (2015).
[32] A. Karim and S. Ahmad, Phys. Rev. C **92**, 064608 (2015).
[33] H. Abusara, A. V. Afanasjev, and P. Ring, Phys. Rev. C **85**, 024314 (2012).
[34] T. Niksšić, D. Vretenar, and P. Ring, Prog. Part. Nucl. Phys. **66**, 519 (2011).
[35] A. V. Afanasjev and H. Abusara, Phys. Rev. C **81**, 014309 (2010).
[36] D. Vretenar, A. V. Afanasjev, G. A. Lalazissis, and P. Ring, Phys. Rep. **409**, 101 (2005).
[37] T. Naz, M. Bhuyan, S. Ahmad, S. K. Patra, and H. Abusara, Nucl. Phys. A **987**, 295 (2019).
[38] H. Abusara and S. Ahmad, Turk. J. Phys. **41**, 203 (2017).
[39] G. A. Lalazissis, S. Karatzikos, R. Fossion, D. Peña Arteaga, A. V. Afanasjev, and P. Ring, Phys. Lett. B **671**, 36 (2009).
[40] Y. K. Gambhir, P. Ring, and A. Thimet, Ann. Phys. (NY) **198**, 132 (1990).
[41] B. B. Serot and J. D. Walecka, in *Advances in Nuclear Physics*, edited by J. W. Negle and E. Vogt, (Plenum, New York, 1986), Vol. 16.
[42] J. D. Walecka, Ann. Phys. (NY) **83**, 491 (1974).
[43] J. Boguta and A. R. Bodmer, Nucl. Phys. A **292**, 413 (1977).
[44] W. Pannert, P. Ring, and J. Boguta, Phys. Rev. Lett. **59**, 2420 (1987).
[45] P. G. Reihard, M. Rufa, J. Maruhn, W. Greiner, and J. Friedrich, Z. Phys. A **323**, 13 (1986).

[46] G. A. Lalazissis, J. König, and P. Ring, Phys. Rev. C **55**, 540 (1997).
[47] B. G. Todd-Rutel and J. Piekarewicz, Phys. Rev. Lett. **95**, 122501 (2005).
[48] P. W. Zhao, Z. P. Li, J. M. Yao, and J. Meng, Phys. Rev. C **82**, 054319 (2010).
[49] B. A. Nikolaus, T. Hoch, and D. G. Madland, Phys. Rev. C **46**, 1757 (1992).
[50] T. Nikšić, N. Paar, D. Vretenar, and P. Ring, Comput. Phys. Commun. **185**, 1808 (2014).
[51] P. Ring, Prog. Part. Nucl. Phys. **37**, 193 (1996).
[52] P. Ring and P. Schuck, *The Nuclear Many-Body Problem*, edited by W. Beiglböck (Springer-Verlag, New York, 1980).
[53] Y. Tian, Z. Y. Ma, and P. Ring, Phys. Lett. B **676**, 44 (2009).
[54] Y. Tian, Z. Y. Ma, and P. Ring, Phys. Rev. C **79**, 064301 (2009).
[55] Y. Tian, Z. Y. Ma, and P. Ring, Phys. Rev. C **80**, 024313 (2009).
[56] T. Nikšić, P. Ring, D. Vretenar, Y. Tian, and Z. Y. Ma, Phys. Rev. C **81**, 054318 (2010).
[57] J. F. Berger, M. Girod, and D. Gogny, Comput. Phys. Commun. **63**, 365 (1991).
[58] A. Staszack, M. Stoitsov, A. Baran, and W. Nazarewicz, Eur. Phys. J. A **46**, 85 (2010).
[59] D.Bonatsos, I. E. Assimakis, N. Minkov, A. Martinou, S. Sarantopoulou, R. B. Cakirli, R. F. Casten, and K. Blaum, Phys. Rev. C **95**, 064326 (2017).
[60] B. Pritychenko, M. Birch, B. Singh, and M. Horoi, At. Data Nucl. Data Tables **107**, 1 (2016).
[61] http://www.nndc.bnl.gov.
[62] I. Angeil and K. P. Marinova, At. Data Nucl. Data Tables **99**, 69 (2013).
[63] H. Abusara, A. V. Afanasjev, and P. Ring, Phys. Rev. C **82**, 044303 (2010).
[64] V.M. Strutinsky, Sov. J. Nucl. Phys. **3**, 449 (1966).